Rapid Communications

Nonsymmorphic Dirac semimetal and carrier dynamics in the doped spin-orbit-coupled Mott insulator Sr_2IrO_4

J. W. Han,[1,*] Sun-Woo Kim,[2,*] W. S. Kyung,[3,4,5] C. Kim,[4,5] G. Cao,[6] X. Chen,[7] S. D. Wilson,[7] Sangmo Cheon,[2,†] and J. S. Lee[1,‡]

[1]*Department of Physics and Photon Science, School of Physics and Chemistry, Gwangju Institute of Science and Technology (GIST), Gwangju 61005, Republic of Korea*

[2]*Department of Physics, Hanyang University, Seoul 04763, Republic of Korea*

[3]*Advanced Light Source, Lawrence Berkeley National Laboratory, Berkeley, California 94720, USA*

[4]*Center for Correlated Electron Systems, Institute for Basic Science (IBS), Seoul 08826, Republic of Korea*

[5]*Department of Physics and Astronomy, Seoul National University (SNU), Seoul 08826, Republic of Korea*

[6]*Department of Physics, University of Colorado, Boulder, Colorado 80309, USA*

[7]*Department of Materials, University of California, Santa Barbara, California 93106, USA*

(Received 30 October 2019; accepted 22 June 2020; published 7 July 2020)

A Dirac fermion emerges as a result of interplay between symmetry and topology in condensed matter. Current research moves towards investigating the Dirac fermions in the presence of many-body effects in correlated systems. Here, we demonstrate the emergence of a correlation-induced symmetry-protected Dirac semimetal state in the lightly doped spin-orbit-coupled Mott insulator Sr_2IrO_4. We find that the nonsymmorphic crystalline symmetry stabilizes a Dirac line-node semimetal and that the correlation-induced symmetry-breaking electronic order further leads to a phase transition from the Dirac line-node to a Dirac point-node semimetal. The latter state is experimentally confirmed by angle-resolved photoemission spectroscopy and terahertz spectroscopy on $Sr_2(Ir, Tb)O_4$ and $(Sr, La)_2IrO_4$. Remarkably, the electrodynamics of the massless Dirac carriers is governed by the extremely small scattering rate of about 6 cm^{-1} even at room temperature, which is iconic behavior of relativistic quasiparticles. Temperature-dependent changes in electrodynamic parameters are also consistently explained based on the Dirac point-node semimetal state.

DOI: 10.1103/PhysRevB.102.041108

Dirac semimetal (DSM) [1] is a new quantum state of matter protected by the interplay of symmetry and topology, and exhibits the electrodynamics of relativistic quasiparticles in a condensed matter system. Such a novel state of quantum matter is described by the massless Dirac equation, and extensive investigations [2–7] have been made about how the Dirac physics incorporates electron correlation and spin-orbit coupling (SOC). When the electron correlation and/or SOC is strong, a Dirac fermion acquires its velocity renormalization [3,4] or mass [5,6]. For instance, a Dirac fermion in graphene near the charge-neutrality point undergoes logarithmic velocity renormalization by long-range Coulomb interaction [3,4] and a Dirac fermion in the correlated kagome magnet becomes massive in the presence of strong SOC [5,6]. The interactions involved determine the fate of the Dirac fermions. It is thus interesting to investigate how the interplay among electron correlation, SOC, and crystalline symmetries affects Dirac fermions. So far, most studies [3–7] of Dirac fermions in a correlated system have been limited to pure (undoped) materials which are inherent metals. Unlike pure systems, a doped correlated system having, for example, the remnant correlations endemic to the parent Mott state [8–12], is particularly promising for seeing the interplay of various kinds of interactions owing to the emergence of a plethora of correlation-induced symmetry-breaking orders [9–12]. In this respect, a doped correlated system hosting Dirac fermions could provide a new window for studying the relatively unexplored realm of correlated Dirac fermions.

Recently, iridates have attracted considerable attention due to the novel correlated and topological phases arising from a delicate combination of electron correlation and SOC [13,14]. Among them, a spin-orbit-coupled Mott insulator Sr_2IrO_4 [15,16] is of particular interest because of its striking similarity to cuprate phenomenology under doping such as Fermi arcs [17,18], a d-wave pseudogap [17–19], and various symmetry-breaking orders [20–23]. Here, by combining theoretical calculations with angle-resolved photoemission spectroscopy (ARPES) and terahertz (THz) spectroscopy on $Sr_2(Ir, Tb)O_4$ and $(Sr, La)_2IrO_4$, we demonstrate that the essential Dirac semimetal protected by nonsymmorphic crystalline symmetry emerges in the lightly doped spin-orbit-coupled Mott insulator Sr_2IrO_4 even in the presence of strong SOC and electron correlation. Remarkably, a correlation-induced symmetry-breaking order leads to a phase transition from a Dirac line node (DLN) to a Dirac point node (DPN). The correlation effect is also manifest in temperature-dependent Dirac carrier dynamics with an extremely small scattering rate, enabling the distinction between DLN and DPN states.

*These two authors contributed equally to this work.
†sangmocheon@hanyang.ac.kr
‡jsl@gist.ac.kr

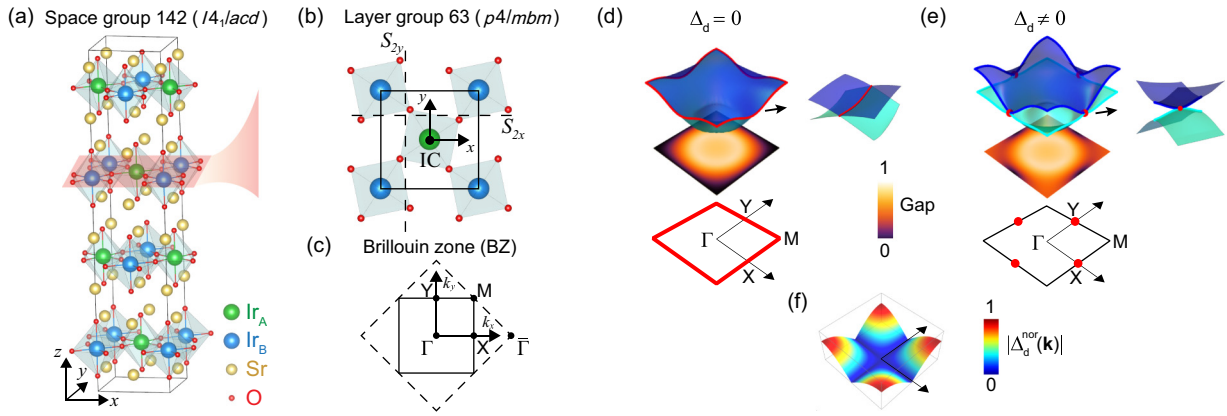

FIG. 1. (a), (b) Crystal structure of layered and single-layer Sr_2IrO_4. (c) BZ for $\sqrt{2} \times \sqrt{2}$ (1 × 1) unit cell drawn by a solid (dashed) line. (d), (e) Calculated 3D band structures of single-layer Sr_2IrO_4 without and with d-wave order. Below each 3D band structure, the 2D contour plot shows the normalized band gap. Red lines and points indicate fourfold degeneracy. (f) Normalized d-wave gap function $\Delta_d^{nor}(\mathbf{k}) = \sin(k_x/2)\sin(k_y/2)$.

Sr_2IrO_4 is a layered compound, where each layer consists of Ir_A and Ir_B sublattices surrounded by oxygen octahedra that are rotated around the z axis in a staggered fashion forming a $\sqrt{2} \times \sqrt{2}$ unit cell [Figs. 1(a) and 1(b)]. Owing to the weak interlayer interaction, Sr_2IrO_4 (space group $I4_1/acd$) is a quasi-two-dimensional (quasi-2D) system whose crystalline symmetries are captured by the layer group $p4/mbm$ [24]. The ground state of Sr_2IrO_4 is an antiferromagnetic Mott insulating state [16]. Upon Tb or La doping [35,38], the antiferromagnetism is strongly suppressed and a metallic state appears even at low doping concentration. For our 3% Tb-doped Sr_2IrO_4 system, $Sr_2(Ir_{0.97}Tb_{0.03})O_4$, it is reported that Tb^{4+} ($4f^7$) ions substitute for Ir^{4+} ions while keeping the crystal symmetry of the parent compound [35]. The isovalent Tb^{4+} dopants do not introduce additional charge carriers and completely suppress the Néel temperature, inducing a paramagnetic metallic state with time-reversal symmetry.

To study the symmetry-protected DSM in $Sr_2(Ir_{0.97}Tb_{0.03})O_4$, we first perform a symmetry analysis for the layer group $p4/mbm$ with time-reversal symmetry. This layer group contains symmetry elements of inversion P, mirror M_z, and two orthogonal nonsymmorphic screw rotations $S_{2x} \equiv \{C_{2x}|\frac{1}{2}00\}$ and $S_{2y} \equiv \{C_{2y}|0\frac{1}{2}0\}$, i.e., a rotation $C_{2x,2y}$ around the x or y axis followed by a translation of half a lattice vector along that x or y axis [Fig. 1(b)]. Note that each rotation axis of nonsymmorphic symmetries S_{2x} and S_{2y} does not intersect an inversion center (IC). This kind of nonsymmorphic symmetry is called off-centered nonsymmorphic symmetry [33,34]. Let us see the role of the single off-centered screw rotation S_{2x}. The commutation relation between P and S_{2x} is given by $PS_{2x} = e^{-ik_x+ik_y}S_{2x}P$, leading to $\{P, S_{2x}\} = 0$ at X and Y points in the Brillouin zone (BZ). Combined with inversion $P^2 = 1$ and time reversal $\Theta^2 = -1$, this symmetry algebra guarantees fourfold-degenerate DPNs at X and Y points [24,33]. With M_z satisfying $\{M_z, S_{2x}\} = 0$, the DPN at the Y point is further spanned as a DLN along the $k_y = \pi$ line [24]. Similarly, S_{2y} with $P\Theta$ and M_z symmetries generates DLN along the $k_x = \pi$ line. Therefore, the multiple symmetries of S_{2x}, S_{2y}, $P\Theta$, and M_z protect the DLN along the whole BZ boundary, which is confirmed by the calculated band structure [Fig. 1(d)].

Next, we consider the electron correlation effect in lightly Tb-doped Mott systems. The most prominent correlated electron phenomenon in lightly doped Mott systems is the emergence of a pseudogap as ubiquitously observed in lightly doped cuprates [10–12]. Indeed, for lightly electron-doped Sr_2IrO_4, a d-wave pseudogap was experimentally observed [17–19] and was plausibly explained by symmetry-breaking electronic order—a so-called d-wave spin-orbit density wave (d-SODW) [22]—in the mean-field level. In a Tb-doped system, we also have experimental evidence for a d-wave pseudogap in ARPES experiment, as we will see. Thus, we introduce d-SODW order with a d-wave form factor $\Delta_d(\mathbf{k}) = -4\Delta_d \sin(k_x/2)\sin(k_y/2)$ [Fig. 1(f)] to consider the electron correlation-induced pseudogap [24].

When the correlation-induced d-wave order is present ($\Delta_d \neq 0$), S_{2x} and S_{2y} symmetries are broken, while M_z and $P\Theta$ symmetries are preserved [24]. This leads to the lifting of the fourfold degeneracy of DLN. However, from the nature of a d-wave form factor [Fig. 1(f)], there are symmetry-invariant lines $k_x = 0$ and $k_y = 0$ where the d-wave order vanishes, that is, S_{2x} and S_{2y} symmetries are still maintained. Hence, at the X and Y points, the previous symmetry algebra for S_{2x} and S_{2y} holds, which guarantees fourfold-degenerate states, i.e., $|\Psi\rangle$, $P|\Psi\rangle$, $\Theta|\Psi\rangle$, and $P\Theta|\Psi\rangle$. Consequently, the electron correlation-induced d-wave order lifts the fourfold degeneracies along the whole BZ boundary, except for the points located at the symmetry-invariant lines, leading to the phase transition from DLN to DPN [Fig. 1(e)] [55]. The relativistic dispersion relation $E = pc$ is established along only the one-dimensional (1D) direction for DLN, whereas a complete 2D relativistic dispersion relation is realized in DPNs. Due to this dimensional discrepancy, differences in physical observables are expected between DLN and DPN states.

For a quantitative comparison with experiment, we calculate the electronic structures of DLN and DPN states using a realistic 2D tight-binding model including SOC with hopping parameters derived from density-functional theory calculations [22]. We treat electron correlation effects within a five-orbital mean-field Hubbard model [24]. Let us first see the electronic structure without d-wave order. In Fig. 2(a), the band structure shows a dispersive DLN along the $\overline{YM}$

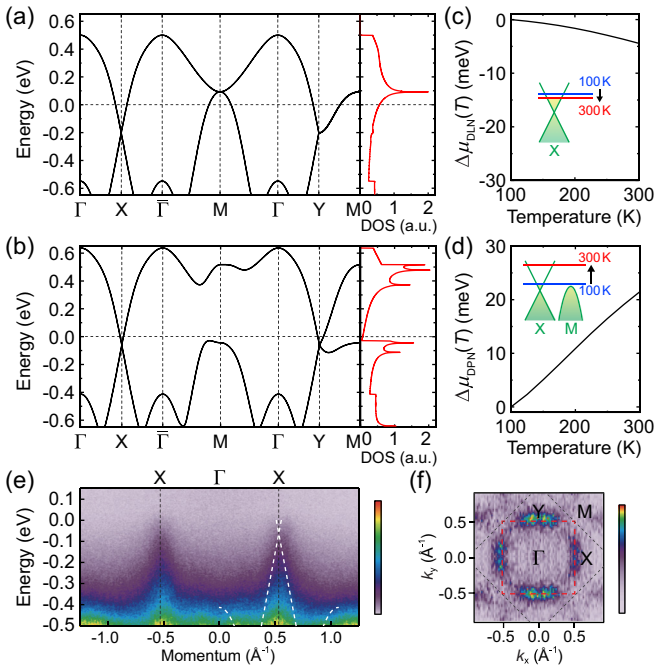

FIG. 2. (a), (b) Calculated band structures and DOS for (a) DLN and (b) DPN states. (c), (d) Calculated T-dependent chemical potentials $\mu(T)$ of (c) DLN and (d) DPN states. (e) ARPES spectra of $Sr_2(Ir_{0.97}Tb_{0.03})O_4$ at 100 K along the X-Γ-X line, which are overlaid with the band structure of the DPN state (white dashed lines). Note that the measured Fermi velocity ($\approx 1/1000c$) agrees well with the theoretical value. (f) Constant binding energy $k_x - k_y$ map at $E = E_F$.

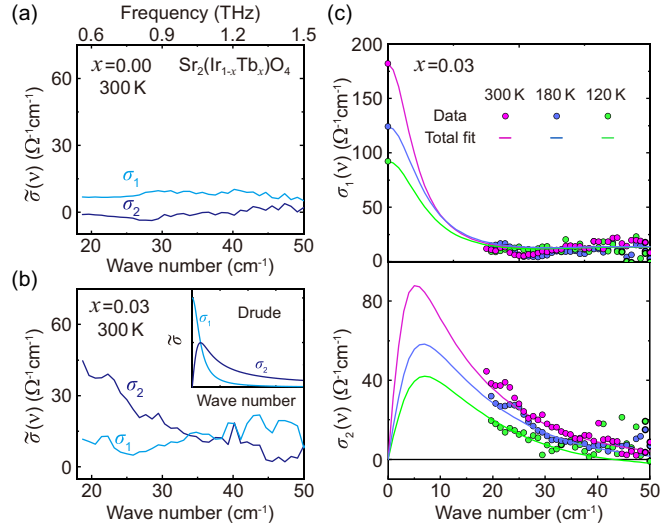

FIG. 3. (a), (b) Real $[\sigma_1(\nu)]$ and imaginary $[\sigma_2(\nu)]$ parts of $\tilde{\sigma}$ obtained at 300 K for (a) $x = 0.00$ and (b) $x = 0.03$. The inset in (b) shows the typical Drude response. (c) $\sigma_1(\nu)$ and $\sigma_2(\nu)$ of $x = 0.03$ at 120, 180, and 300 K. Symbols at zero wave number indicate the DC conductivity values obtained from the transport measurement [35]. Solid lines are Drude-Lorentz fitting results where each contribution of Drude and Lorentz response is presented in the Supplemental Material [24].

line. At the M point, two parabolic bands meet, leading to a van Hove singularity (vHs) near energy $E = 0.1$ eV, as shown in the density of states (DOS). Meanwhile, the correlation-induced d-wave order lifts the degeneracy of DLN along the BZ boundary, forming anisotropic DPNs at the X and Y points [Figs. 1(e) and 2(b)]. At the M point, the two parabolic bands become gapped with an energy gap of ∼0.4 eV, generating several vHs as shown in DOS [Fig. 2(b)]. The correlation-induced vHs near the Fermi level ($E \sim -0.04$ eV), in particular, gives rise to an unconventional temperature- (T-) dependent chemical potential. Calculated chemical potentials $\mu_{DLN}(T)$ and $\mu_{DPN}(T)$ of DLN and DPN states show the opposite T dependence [Figs. 2(c) and 2(d)]. In this case, $\mu_{DLN}(T)$ decreases with increasing T. On the other hand, $\mu_{DPN}(T)$ is proportional to T—different from $\mu(T)$ of graphene [Fig. S18(a) in [24]]—because the correlation-induced heavy hole band at the M point acts as an effective carrier reservoir supplying electrons to the Dirac band. Note that these chemical potentials of DLN and DPN states are essential ingredients for determining differences in T-dependent Dirac carrier dynamics.

Before addressing Dirac carrier dynamics, we identify the electronic structure of $Sr_2(Ir_{0.97}Tb_{0.03})O_4$ using ARPES. As shown in Fig. 2(e), Dirac-like linear dispersion is observed up to the Fermi level with a Dirac point at the X point with the binding energy ∼50 meV (see also Supplemental Material [24]). The 2D ARPES map in Fig. 2(f) shows a clear d-wave pseudogap feature, namely, a gap at the M point and nodal regions around the X and Y points, which is similar to that observed in electron-doped Sr_2IrO_4 [17–19]. These ARPES results are consistent with the calculated band structure with d-wave order in Fig. 2(b). Therefore, the ARPES data support the emergence of the DPN state rather than the DLN state [59].

Next, we study Dirac carrier dynamics and further distinguish the electronic states of Tb-doped Sr_2IrO_4 based on THz spectroscopy. To figure out changes of carrier dynamics upon Tb doping, we first study the Mott insulating state of the parent Sr_2IrO_4 at 300 K [Fig. 3(a)]. The real part $\sigma_1(\nu)$ of the optical conductivity $\tilde{\sigma}(\nu)$ shows a featureless spectral response from 20 to 50 cm^{-1} with a successful connection to the DC conductivity $\sigma_{DC} \sim 10\ \Omega^{-1}\,cm^{-1}$ [35]. Similarly, the imaginary part $\sigma_2(\nu)$ shows a flat spectrum. These spectral features are consistent with the Mott insulating state of the parent compound [63]. For $Sr_2(Ir_{0.97}Tb_{0.03})O_4$ [Fig. 3(b)], $\sigma_1(\nu)$ rises slightly with increasing frequency. In contrast to the parent Sr_2IrO_4, a significant increase of $\sigma_1(\nu)$ at $< 20\ cm^{-1}$ is expected because $\sigma_{DC} = 180\ \Omega^{-1}\,cm^{-1}$ [Fig. 3(c)]. Consistently, $\sigma_2(\nu)$ increases with decreasing frequency. These spectral observations are reminiscent of the high-frequency tail of the Drude response; wide spectral features of the Drude peak are displayed in the inset of Fig. 3(b). It should be noted that the scattering rate defined in the Drude model corresponds to the half-width of σ_1 and the extremal point frequency of σ_2, or equivalently the crossing point of σ_1 and σ_2. In these respects, the results in Fig. 3(b) clearly indicate that the free-carrier scattering rate is given to be far less than 20 cm^{-1}.

We employ the Drude-Lorentz model to analyze $\tilde{\sigma}(\nu)$ and extract two important electrodynamics parameters: The scattering rate γ and the Drude weight D. We verify the validity of the model detailed in the Supplemental Material

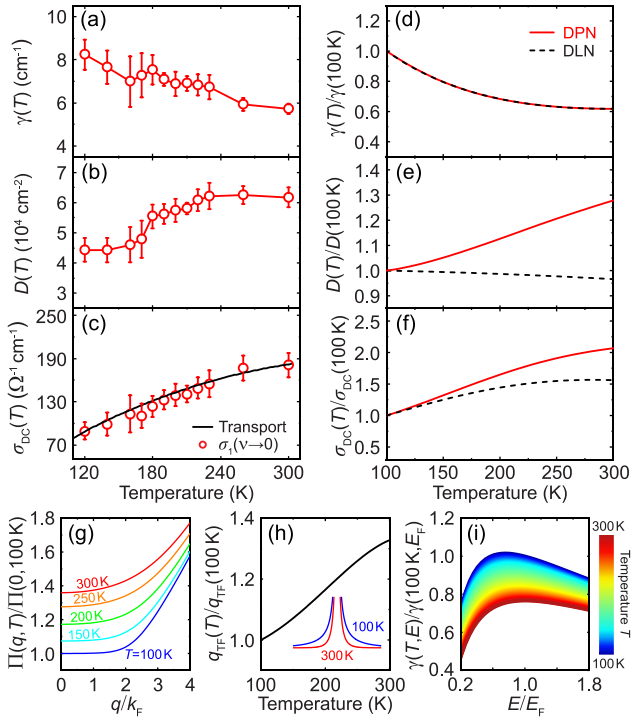

FIG. 4. (a), (b) Experimentally obtained scattering rate $\gamma(T)$ and Drude weight $D(T)$. (c) DC conductivity $\sigma_{\rm DC}(T)$ estimated by Drude analysis (symbol) and directly acquired by transport measurement (line). (d)–(f) Theoretically obtained $\gamma(T)$, $D(T)$, and $\sigma_{\rm DC}(T)$ [24]. (g)–(i) Calculated polarizability function $\Pi(q,T)$, Thomas-Fermi wave vector $q_{\rm TF}(T)$, and RPA scattering rate $\gamma(T,E)$ for the DPN state [24].

[24]. Note that the fitting has been performed by satisfying $\sigma_1(\nu)$, $\sigma_2(\nu)$, and $\sigma_{\rm DC}$ simultaneously. At 300 K, we obtain $\gamma = 5.8\ {\rm cm}^{-1}$ and $D = 62\,500\ {\rm cm}^{-2}$ [Fig. 3(c)]. It is worth emphasizing that the observed γ is extremely small even at room temperature, and it is one of the key fingerprints of Dirac fermions; γ is significantly reduced due to the large Fermi velocity and the chiral nature of massless Dirac fermions [64,65]. Similar small values of γ have been reported for several DSMs [49,66,67]. For a 2D DSM, the suspended graphene [49] exhibits $\gamma \approx 20\ {\rm cm}^{-1}$ at 40 K. For a 3D DSM, $ZrTe_5$ [66] and Cd_3As_2 [67] show $\gamma \approx 13$ and $10\ {\rm cm}^{-1}$ at 200 and 300 K, respectively.

As discussed before, differences in T-dependent carrier dynamics between DLN and DPN states are expected, and hence THz optical spectra are examined in detail with varying T. In Fig. 3(c), we compare $\tilde{\sigma}(\nu)$ obtained at 120, 180, and 300 K. $\sigma_1(\nu)$ does not show a noticeable T-dependent spectral change. However, $\sigma_2(\nu)$ becomes larger with increasing T, thereby showing the systematic increase of the spectral weight. We fit all measured $\tilde{\sigma}(\nu)$ [24] and obtain T-dependent scattering rate $\gamma(T)$ and Drude weight $D(T)$ as displayed in Figs. 4(a) and 4(b), respectively. $\gamma(T)$ decreases with increasing T and a very small $\gamma(T)$ is observed over a wide T range, consistent with the fact that a symmetry-protected Dirac semimetallic state is robust against thermal effect. $D(T)$ increases with increasing T. Thus, the combination of $\gamma(T)$ and $D(T)$ leads to the rise of $\sigma_1(\nu \to 0)$ with increasing T, in good agreement with the transport data shown in Fig. 4(c).

To understand the THz data measured, we calculate the T-dependent optical conductivity using the Boltzmann transport equation [24]. For scattering mechanisms in Dirac systems (e.g., graphene), one can consider both phonon and charged impurity scatterings [65]. However, decreasing $\gamma(T)$ with increasing T [Fig. 4(a)] cannot be explained by phonons which inevitably result in increasing $\gamma(T)$ with increasing T. Thus, we focus on the charged impurity scattering and consider two types of charged impurities depending on the nature of their Coulomb potentials: Short-range and long-range charged impurities. By combining these two charged impurities, we construct a phenomenological model for the scattering rate $\gamma_{\rm model}(T,E)$ as described in the Supplemental Material [24]. Then, using $\gamma_{\rm model}(T,E)$ as input, we calculate $\gamma(T)$ for the DLN and the DPN [Fig. 4(d)] such that the calculated $\gamma(T)$ for both the DLN and the DPN are well matched with the experimental values in Fig. 4(a). With the same $\gamma(T)$ values, the calculated $\sigma_{\rm DC}(T)$ for the DLN and the DPN show a qualitatively similar tendency with T [Fig. 4(f)], which means that $\sigma_{\rm DC}(T)$ alone is insufficient to distinguish between the DLN and the DPN. Instead, as shown in Fig. 4(e), the calculated $D(T)$ for the DLN and the DPN show the opposite T dependence; $D(T)$ for the DPN exhibits a consistent T dependence with the experimental result [Fig. 4(b)]. This is mainly due to the different T-dependent chemical potentials between the DLN and the DPN [Figs. 2(c) and 2(d)]. Upon increasing T, $\mu_{\rm DPN}(T)$ increases but $\mu_{\rm DLN}(T)$ decreases, which gives rise to the increase or decrease of the Dirac carrier density, and equivalently, of the $D(T)$. Thus, from the $D(T)$ result, we conclude that the THz experiment supports the emergence of the DPN state rather than the DLN state, consistently with the ARPES experiment.

To study the microscopic scattering mechanism in the DPN state of Tb-doped systems, we scrutinize the finite-temperature screening effect arising from Dirac fermions around charged impurities using random phase approximation (RPA). Within RPA, the static dielectric function $\epsilon(q,T)$ is given by $\epsilon(q,T) = 1 + v_c(q)\Pi(q,T)$ where $v_c(q) = 2\pi e^2/\kappa q$ with the effective dielectric constant κ and $\Pi(q,T)$ is the finite-temperature polarizability function [24,48]. In Fig. 4(g), the calculated $\Pi(q,T)$ increases monotonically with temperature at all q owing to the thermal excitation of Dirac fermions from the valence band to the conduction band. Thus, the Coulomb potential is more screened with increasing T, which is characterized by the Thomas-Fermi screening wave vector $q_{\rm TF}(T) \equiv \lim_{q\to 0} q v_c \Pi(q,T)$ [Fig. 4(h)]. With this $q_{\rm TF}(T)$, we calculate the T- and E-dependent scattering rate $\gamma(T,E)$ [Fig. 4(i)]; $\gamma(T,E)$ decreases with increasing T at all E because the scattering cross section is reduced by enhanced screening of the Coulomb potential, which explains the experimental data in Fig. 4(a). This insulating behavior of $\gamma(T,E)$ is analogous to the high-temperature behavior of $\gamma_{\rm gr}(T,E)$ in high-mobility graphene [24,48,49]. Note that the calculated electrodynamic parameters using $\gamma(T,E)$ are consistent with both experimental and theoretical data in Fig. 4 [24].

To generalize the emergence of correlated DSMs in the lightly doped Mott insulator Sr_2IrO_4, we also study a 5.5%

La-doped system, $(Sr_{0.945}La_{0.055})_2IrO_4$. Because it has the same crystal structure and magnetic state as the Tb-doped system, the same symmetry analysis with d-wave order can be applied. Indeed, Dirac dispersion and a d-wave pseudogap were observed by ARPES for $(Sr_{0.95}La_{0.05})_2IrO_4$ [19], suggesting that it has a DPN ground state. From the THz experiment on $(Sr_{0.945}La_{0.055})_2IrO_4$, we obtain an extremely small scattering rate of $\sim 4\ cm^{-1}$ at room T [24], which is the direct manifestation of Dirac carrier dynamics.

In summary, we demonstrated the universal emergence of nonsymmorphic Dirac semimetal with point-node dispersion in the lightly doped spin-orbit-coupled Mott insulator Sr_2IrO_4. The interplay between nonsymmorphic symmetry and correlation-induced symmetry-breaking electronic order is essential in realizing Dirac point-node semimetal. Such Dirac semimetal allows the relativistic electrodynamics governed by the extremely small scattering rate even at room temperature, thus providing an intriguing opportunity to explore new emergent and collective phenomena of correlated Dirac materials.

This work was supported by the Science Research Center and the Basic Science Research Program through the National Research Foundation of Korea (NRF) funded by the Ministry of Science, ICT and Future Planning (Grants No. 2015R1A5A1009962 and No. 2018R1A2B2005331). S.-W.K. and S.C. were supported by NRF through Basic Science Research Programs (Grant No. NRF-2018R1C1B6007607), the research fund of Hanyang University (HY-2017), and the POSCO Science Fellowship of POSCO TJ Park Foundation. W.S.K and C.K. were supported by the Institute for Basic Science in Korea (Grant No. IBS-R009-G2). S.D.W. and X.C. acknowledge support from NSF Award No. DMR-1905801. G.C. acknowledges NSF support via grant DMR-1903888.

[1] N. P. Armitage, E. J. Mele, and A. Vishwanath, Rev. Mod. Phys. **90**, 015001 (2018).
[2] V. N. Kotov, B. Uchoa, V. M. Pereira, F. Guinea, and A. H. Castro Neto, Rev. Mod. Phys. **84**, 1067 (2012).
[3] D. C. Elias, R. V. Gorbachev, A. S. Mayorov, S. V. Morozov, A. A. Zhukov, P. Blake, L. A. Ponomarenko, I. V. Grigorieva, K. S. Novoselov, F. Guinea, and A. K. Geim, Nat. Phys. **7**, 701 (2011).
[4] H.-K. Tang, J. N. Leaw, J. N. B. Rodrigues, I. F. Herbut, P. Sengupta, F. F. Assaad, and S. Adam, Science **361**, 570 (2018).
[5] L. Ye, M. Kang, J. Liu, F. von Cube, C. R. Wicker, T. Suzuki, C. Jozwiak, A. Bostwick, E. Rotenberg, D. C. Bell, L. Fu, R. Comin, and J. G. Checkelsky, Nature (London) **555**, 638 (2018).
[6] J.-X. Yin, S. S. Zhang, H. Li, K. Jiang, G. Chang, B. Zhang, B. Lian, C. Xiang, I. Belopolski, H. Zheng, T. A. Cochran, S.-Y. Xu, G. Bian, K. Liu, T.-R. Chang, H. Lin, Z.-Y. Lu, Z. Wang, S. Jia, W. Wang, and M. Z. Hasan, Nature (London) **562**, 91 (2018).
[7] J. Fujioka, R. Yamada, M. Kawamura, S. Sakai, M. Hirayama, R. Arita, T. Okawa, D. Hashizume, M. Hoshino, and Y. Tokura, Nat. Commun. **10**, 362 (2019).
[8] M. Imada, A. Fujimori, and Y. Tokura, Rev. Mod. Phys. **70**, 1039 (1998).
[9] S. Chakravarty, R. B. Laughlin, D. K. Morr, and C. Nayak, Phys. Rev. B **63**, 094503 (2001).
[10] P. A. Lee, N. Nagaosa, and X.-G. Wen, Rev. Mod. Phys. **78**, 17 (2006).
[11] B. Keimer, S. A. Kivelson, M. R. Norman, S. Uchida, and J. Zaanen, Nature (London) **518**, 179 (2015).
[12] E. Fradkin, S. A. Kivelson, and J. M. Tranquada, Rev. Mod. Phys. **87**, 457 (2015).
[13] W. Witczak-Krempa, G. Chen, Y. B. Kim, and L. Balents, Annu. Rev. Condens. Matter Phys. **5**, 57 (2014).
[14] J. G. Rau, E. K.-H. Lee, and H.-Y. Kee, Annu. Rev. Condens. Matter Phys. **7**, 195 (2016).
[15] B. J. Kim, H. Jin, S. J. Moon, J.-Y. Kim, B.-G. Park, C. S. Leem, J. Yu, T. W. Noh, C. Kim, S.-J. Oh, J.-H. Park, V. Durairaj, G. Cao, and E. Rotenberg, Phys. Rev. Lett. **101**, 076402 (2008).
[16] B. J. Kim, H. Ohsumi, T. Komesu, S. Sakai, T. Morita, H. Takagi, and T. Arima, Science **323**, 1329 (2009).
[17] Y. K. Kim, O. Krupin, J. D. Denlinger, A. Bostwick, E. Rotenberg, Q. Zhao, J. F. Mitchell, J. W. Allen, and B. J. Kim, Science **345**, 187 (2014).
[18] Y. K. Kim, N. H. Sung, J. D. Denlinger, and B. J. Kim, Nat. Phys. **12**, 37 (2016).
[19] A. de la Torre, S. McKeown Walker, F. Y. Bruno, S. Riccó, Z. Wang, I. Gutierrez Lezama, G. Scheerer, G. Giriat, D. Jaccard, C. Berthod, T. K. Kim, M. Hoesch, E. C. Hunter, R. S. Perry, A. Tamai, and F. Baumberger, Phys. Rev. Lett. **115**, 176402 (2015).
[20] L. Zhao, D. H. Torchinsky, H. Chu, V. Ivanov, R. Lifshitz, R. Flint, T. Qi, G. Cao, and D. Hsieh, Nat. Phys. **12**, 32 (2016).
[21] I. Battisti, K. M. Bastiaans, V. Fedoseev, A. de la Torre, N. Iliopoulos, A. Tamai, E. C. Hunter, R. S. Perry, J. Zaanen, F. Baumberger, and M. P. Allan, Nat. Phys. **13**, 21 (2017).
[22] S. Zhou, K. Jiang, H. Chen, and Z. Wang, Phys. Rev. X **7**, 041018 (2017).
[23] X. Chen, J. L. Schmehr, Z. Islam, Z. Porter, E. Zoghlin, K. Finkelstein, J. P. C. Ruff, and S. D. Wilson, Nat. Commun. **9**, 103 (2018).
[24] See Supplemental Material at http://link.aps.org/supplemental/10.1103/PhysRevB.102.041108 for a discussion of symmetry analysis, model Hamiltonian, sample preparation, ARPES results, details of THz experiments, extraction of D and γ from the Drude-Lorentz fitting, Boltzmann transport theory for optical properties of the DPN state, comparison with graphene, and THz data and theoretical analysis on the La-doped sample, which includes Refs. [17–19,22,25–54].
[25] M. K. Crawford, M. A. Subramanian, R. L. Harlow, J. A. Fernandez-Baca, Z. R. Wang, and D. C. Johnston, Phys. Rev. B **49**, 9198 (1994).
[26] D. H. Torchinsky, H. Chu, L. Zhao, N. B. Perkins, Y. Sizyuk, T. Qi, G. Cao, and D. Hsieh, Phys. Rev. Lett. **114**, 096404 (2015).
[27] G. Kresse and J. Hafner, Phys. Rev. B **48**, 13115 (1993).
[28] G. Kresse and J. Furthmüller, Comput. Mater. Sci. **6**, 15 (1996).
[29] J. P. Perdew, K. Burke, and M. Ernzerhof, Phys. Rev. Lett. **77**, 3865 (1996).

[30] P. Liu, M. Reticcioli, B. Kim, A. Continenza, G. Kresse, D. D. Sarma, X.-Q. Chen, and C. Franchini, Phys. Rev. B **94**, 195145 (2016).
[31] F. Ye, S. Chi, B. C. Chakoumakos, J. A. Fernandez-Baca, T. Qi, and G. Cao, Phys. Rev. B **87**, 140406(R) (2013).
[32] F. Ye, X. Wang, C. Hoffmann, J. Wang, S. Chi, M. Matsuda, B. C. Chakoumakos, J. A. Fernandez-Baca, and G. Cao, Phys. Rev. B **92**, 201112(R) (2015).
[33] B. J. Wieder and C. L. Kane, Phys. Rev. B **94**, 155108 (2016).
[34] B.-J. Yang, T. A. Bojesen, T. Morimoto, and A. Furusaki, Phys. Rev. B **95**, 075135 (2017).
[35] J. C. Wang, S. Aswartham, F. Ye, J. Terzic, H. Zheng, D. Haskel, S. Chikara, Y. Choi, P. Schlottmann, R. Custelcean, S. J. Yuan, and G. Cao, Phys. Rev. B **92**, 214411 (2015).
[36] N. H. Sung, H. Gretarsson, D. Proepper, J. Porras, M. L. Tacon, A. V. Boris, B. Keimer, and B. J. Kim, Philos. Mag. **96**, 413 (2016).
[37] J.-M. Carter, V. Shankar V., and H.-Y. Kee, Phys. Rev. B **88**, 035111 (2013).
[38] X. Chen, T. Hogan, D. Walkup, W. Zhou, M. Pokharel, M. Yao, W. Tian, T. Z. Ward, Y. Zhao, D. Parshall, C. Opeil, J. W. Lynn, V. Madhavan, and S. D. Wilson, Phys. Rev. B **92**, 075125 (2015).
[39] T. B. Boykin and G. Klimeck, Phys. Rev. B **71**, 115215 (2005).
[40] P. Gu, M. Tani, S. Kono, K. Sakai, and X.-C. Zhang, J. Appl. Phys. **91**, 5533 (2002).
[41] J. W. Han, S. Y. Hamh, T. H. Kim, K. S. Lee, N. E. Yu, D.-K. Ko, and J. S. Lee, Opt. Lett. **39**, 5531 (2014).
[42] J. W. Han, M. S. Kim, M. S. Song, B. Y. Kang, B. K. Cho, and J. S. Lee, Appl. Opt. **56**, 2529 (2017).
[43] J. W. Han, Y. G. Choi, and J. S. Lee, Sci. Rep. **8**, 6513 (2018).
[44] J. W. Han, Y. G. Choi, and J. S. Lee, J. Opt. Soc. Am. B **36**, 1551 (2019).
[45] S. J. Moon, H. Jin, W. S. Choi, J. S. Lee, S. S. A. Seo, J. Yu, G. Cao, T. W. Noh, and Y. S. Lee, Phys. Rev. B **80**, 195110 (2009).
[46] Y. Liu, T. Low, and P. P. Ruden, Phys. Rev. B **93**, 165402 (2016).
[47] S. Park, S. Woo, E. J. Mele, and H. Min, Phys. Rev. B **95**, 161113(R) (2017).
[48] E. H. Hwang and S. Das Sarma, Phys. Rev. B **79**, 165404 (2009).
[49] K. I. Bolotin, K. J. Sikes, J. Hone, H. L. Stormer, and P. Kim, Phys. Rev. Lett. **101**, 096802 (2008).
[50] K. Lee, A. J. Heeger, and Y. Cao, Phys. Rev. B **48**, 14884 (1993).
[51] G. Tzamalis, N. A. Zaidi, C. C. Homes, and A. P. Monkman, Phys. Rev. B **66**, 085202 (2002).
[52] K. W. Kim, J. S. Lee, T. W. Noh, S. R. Lee, and K. Char, Phys. Rev. B **71**, 125104 (2005).
[53] D. G. Cooke, F. A. Hegmann, E. C. Young, and T. Tiedje, Appl. Phys. Lett. **89**, 122103 (2006).
[54] H. Hempel, A. Redinger, I. Repins, C. Moisan, G. Larramona, G. Dennler, M. Handwerg, S. F. Fischer, R. Eichberger, and T. Unold, J. Appl. Phys. **120**, 175302 (2016).
[55] Note that, unlike the (band-inverted) topological DSMs, these (symmetry-protected) nonsymmorphic DLNs and DPNs have no topological surface state [56–58].
[56] B.-J. Yang and N. Nagaosa, Nat. Commun. **5**, 4898 (2014).
[57] S. M. Young and C. L. Kane, Phys. Rev. Lett. **115**, 126803 (2015).
[58] Y.-T. Oh, H.-G. Min, and Y. Kim, Phys. Rev. B **99**, 201110(R) (2019).
[59] Contrasting to the DPN state of the Tb-doped Sr_2IrO_4, we note that Sr_2RhO_4, a paramagnetic metallic counterpart [60] of Sr_2IrO_4, exhibits the Dirac-like linear dispersion at the X point without the pseudogap (see ARPES data in Refs. [61,62]), thereby implying the DLN state.
[60] J.-H. Park, S. H. Lee, C. H. Kim, H. Jin, and B.-J. Yang, Phys. Rev. B **99**, 195107 (2019).
[61] B. J. Kim, J. Yu, H. Koh, I. Nagai, S. I. Ikeda, S.-J. Oh, and C. Kim, Phys. Rev. Lett. **97**, 106401 (2006).
[62] J. Kwon, M. Kim, D. Song, Y. Yoshida, J. Denlinger, W. Kyung, and C. Kim, Phys. Rev. Lett. **123**, 106401 (2019).
[63] S. J. Moon, H. Jin, K. W. Kim, W. S. Choi, Y. S. Lee, J. Yu, G. Cao, A. Sumi, H. Funakubo, C. Bernhard, and T. W. Noh, Phys. Rev. Lett. **101**, 226402 (2008).
[64] A. H. Castro Neto, F. Guinea, N. M. R. Peres, K. S. Novoselov, and A. K. Geim, Rev. Mod. Phys. **81**, 109 (2009).
[65] S. Das Sarma, S. Adam, E. H. Hwang, and E. Rossi, Rev. Mod. Phys. **83**, 407 (2011).
[66] R. Y. Chen, S. J. Zhang, J. A. Schneeloch, C. Zhang, Q. Li, G. D. Gu, and N. L. Wang, Phys. Rev. B **92**, 075107 (2015).
[67] I. Crassee, E. Martino, C. C. Homes, O. Caha, J. Novák, P. Tückmantel, M. Hakl, A. Nateprov, E. Arushanov, Q. D. Gibson, R. J. Cava, S. M. Koohpayeh, K. E. Arpino, T. M. McQueen, M. Orlita, and A. Akrap, Phys. Rev. B **97**, 125204 (2018).